Exploiting the entire near-infrared spectral range to improve the detection of methane plumes with high-resolution imaging spectrometers

Javier Roger[1], Luis Guanter[1,2], Javier Gorroño[1], and Itziar Irakulis-Loitxate[1,3]

[1]Research Institute of Water and Environmental Engineering (IIAMA), Universitat Politècnica de València (UPV), 46022, Valencia, Spain.
[2]Environmental Defense Fund, Reguliersgracht 79, 1017 LN Amsterdam, The Netherlands.
[3]International Methane Emission Observatory (IMEO), United Nations Environment Programme, Paris, France.

Correspondence: Javier Roger (jarojua@upvnet.upv.es)

Abstract.

Remote sensing ~~has emerged~~ emerges as an important tool for the detection of methane plumes emitted by so-called point sources, which are common in the energy sector (e.g., oil and gas extraction and coal mining activities). In particular, satellite imaging spectroscopy missions covering the shortwave infrared part of the solar spectrum ~~, such as PRISMA, EnMAP~~
~~or GaoFen-5 AHSI, have proven~~ are very effective for this application. These instruments sample the methane absorption features at the spectral regions around 1700 and 2300 nm, which enables the retrieval of per-pixel methane concentration enhancements. Data-driven retrieval methods, in particular those based on the matched filter concept, are widely used to produce maps of methane concentration enhancements from imaging spectroscopy data. ~~These maps are being used for~~ Using these maps enables the detection of plumes and the subsequent identification of active sources. However, retrieval artifacts caused by particular surface components may sometimes appear as false plumes or disturbing elements in the methane maps, which complicates the identification of real plumes. In this work, we ~~have used~~ use a matched filter that exploits a wide spectral window (1000-2500 nm) instead of the usual 2100-2450 nm window with the aim of reducing the occurrence of retrieval artifacts and background noise. This enables a greater ability to discriminate between surface elements and methane. The improvement in plume detection is evaluated through an analysis derived from both simulated data and real data from areas including active point sources, such as the O&G industry from ~~the Permian Basin~~ San Joaquin Valley (U.S.) and the coal mines from the Shanxi region (China). ~~Data sets~~ We use datasets from the PRISMA ~~, and~~ EnMAP ~~, GF5-02~~ satellite imaging spectrometers missions and from the airborne AVIRIS-NG instrument ~~are used. Results~~. We obtain that the interference with atmospheric carbon dioxide and water vapor is generally almost negligible, while coemission or overlapping of these trace gases with methane plumes leads to a reduction of the retrieved concentration values. Attenuation will also occur in the case of methane emissions situated above surface structures that are associated with retrieval artifacts. The results show that the new approach ~~reduces~~ is an optimal trade-off between the reduction of background noise and ~~can remove a great fraction of the~~ retrieval artifacts. ~~For example, the analysis of a scene from the Shanxi region reveals that~~ This is illustrated by a comprehensive analysis in a PRISMA dataset with 15 ~~plumes could be detected from the proposed procedure, whereas only 5 had been identified using~~

~~the classical matched filter applied to the 2300 nm window. In addition, plume masking derived from this new approach let us~~ ~~propose a new procedure for point source quantification optimized for flux rates values ≤ 1000~~ identified plumes, where the output mask from an automatic detection algorithm show an important reduction in the number of clusters not related to CH$_4$ emissions.

1 Introduction

Since pre-industrial times, the concentration of methane (CH$_4$) in the atmosphere has increased by more than 150% to a globally-averaged value of 1920 ~~ppb~~ parts-per-billion (ppb) in early 2023 (Dlugokencky, 2023). CH$_4$ is the second most important anthropogenic greenhouse gas and has been estimated as responsible for almost a third of the warming of the planet so far (Masood et al., 2021). In addition, because of its short lifetime and its a relatively fast mitigation potential (Ocko et al., 2021), reducing atmospheric CH$_4$ concentration is the most efficient way to curb global warming (Ming et al., 2022).

A great portion of the increase in CH$_4$ concentration in the atmosphere is due to the growth of anthropogenic emissions from sectors such as agriculture, waste management, coal mining and the oil and gas (O&G) industry. The O&G industry produces approximately 33% of total anthropogenic emissions and has been identified as one of the sectors with the highest potential to reduce emissions (UNEP, 2021), which is also generally considered cost-effective (Mayfield et al., 2017).

An important fraction of the emissions from fossil fuels ~~come~~ comes from CH$_4$ point sources (Duren et al., 2019). In this context, satellites have proven to be instrumental in detecting CH$_4$ plumes originated in this manner. Especially, satellite imaging spectrometers can leverage the CH$_4$ absorption features in the shortwave infrared (SWIR), where there is a weak ~~(~~ and a strong absorption window around the 1700 nm ~~) and strong (~~ and 2300 nm ~~) absorption window~~ spectral wavelengths (λ), respectively (see Figure 1). Spaceborne measurements of the solar radiation reflected by the Earth's surface can be used to derive CH$_4$ concentration enhancements from these features.

Imaging spectrometers, also known as hyperspectral imagers, have a coarse temporal resolution but offer a ~~high~~ spatial and spectral resolution able to resolve a large range of point sources (Irakulis-Loitxate et al., 2021). Of this kind, we ~~find~~ highlight the Italian PRISMA (Precursore IperSpettrale della Missionse Applicativa) mission (Loizzo et al., 2018) ~~, the Chinese GF5-02 AHSI (GaoFen-5-02 Advanced HyperSpectral Imagers) mission (?),~~ and the German EnMAP (German Environmental Mapping and Analysis Program) mission (Guanter et al., 2015), ~~the three of them~~ both with a 30 m spatial resolution~~and~~, a spectral resolution ~10 nm~~with~~, and a spectral coverage of 400-2500 nm. We ~~can also find~~ also acknowledge the constellation of GHGSat, which have a ~~high~~ spatial resolution varying between 25 and 50 m (depending on the satellite). These satellites have built-in Fabry-Pérot spectrometers that operate only in the 1700 nm CH$_4$ absorption window with a spectral resolution of 0.1 nm (Jervis et al., 2021).

In the existing literature, two types of methodologies have been ~~used to obtain the~~ employed for deriving CH$_4$ concentration ~~in the scene. First, the so-called~~ maps. The first category consists of physically-based methods, which require ~~an exhaustive knowledge about~~ a comprehensive understanding of radiation, its interactions~~and the media that travels through . And there are also~~, and the properties of the medium through which it propagates. On the other hand, data-driven methods ~~, which~~
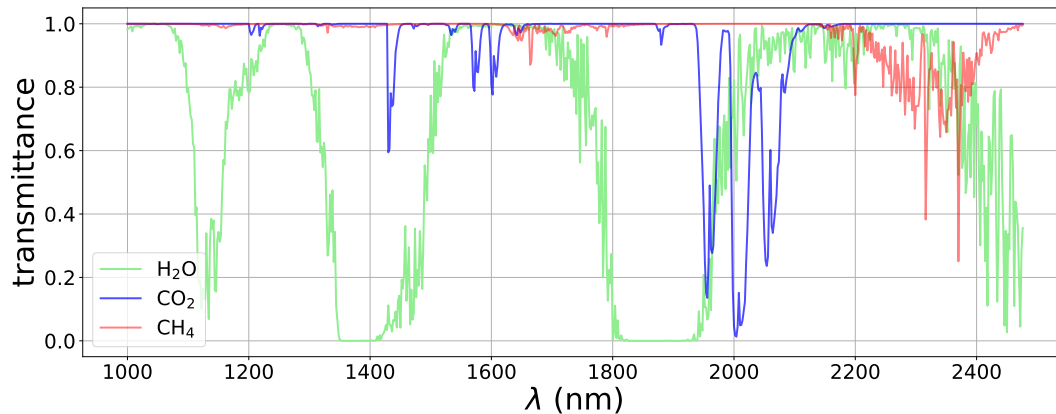
Figure 1. ~~HITRAN~~ MODTRAN derived $transmittance$ spectra of atmospheric H_2O (green), CO_2 (blue), and CH_4 (red) resampled to 2 nm spectral resolution.

~~statistically derive information~~ extract information statistically from the image~~itself. The latter type presents lower~~, offering advantages such as reduced computational time and ~~partially compensates~~ partial compensation for radiometric and spectral errors (Thompson et al., 2015; Guanter et al., 2021). Among the possible methods of this class we ~~can find~~ highlight the matched filter.

The matched filter applied to the CH_4 case maximizes the score on the pixels that most strongly match the CH_4 absorption spectrum (Manolakis et al., 2007) convolved to the spectral response of the satellite sensor, and the bands selected from the ~~data set~~ dataset are usually those covering the 2300 nm absorption window (2100-2450 nm). Unfortunately, the ~~raw~~ matched filter is prone to disturbing enhancements caused by measurement noise and sensitivity to the surface. Specifically, surface elements with similar absorptive features to CH_4 may lead to systematic errors (Thorpe et al., 2013; Ayasse et al., 2018; Guanter et al., 2021). These can be abundantly present in heterogeneous scenes and can ~~difficult~~ complicate or mislead the detection of CH_4 plumes. We show an example in Figure 2. The identification of real CH_4 plumes is complicated because of the large number of these disturbing elements across the scene. Therefore, it is necessary to develop new procedures that get to remove them, and consequently, improve the ability to detect CH_4 emissions.

In this work, we ~~have elaborated~~ present a matched filter-based retrieval that exploits the whole SWIR spectral region with the aim of improving the detection of CH_4 plumes emitted from point-sources. We implement end-to-end simulations from trace gases to test if atmospheric carbon dioxide (CO_2) and water vapor (H_2O) disturb the CH_4 retrieval when ~~extending~~ expanding the spectral range~~, and show~~. Moreover, we present CH_4 concentration enhancement maps derived from both simulated and real data~~that are compared to~~. These maps are compared with other state-of-the-art retrieval ~~. Finally, we test the point-source quantification based on a plume masking resulting from this new approach~~methods, and the plume detection capability is analyzed.
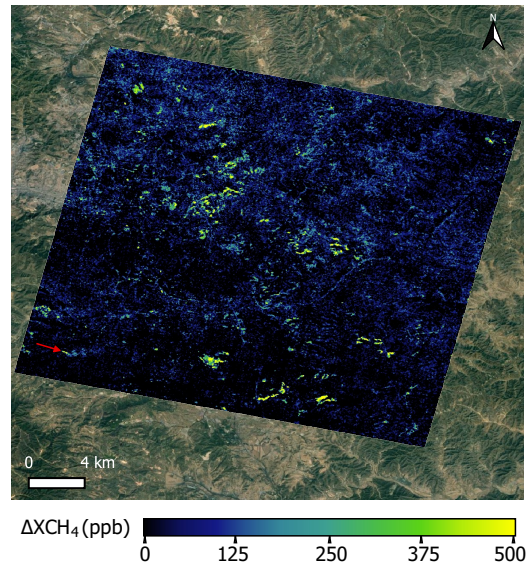
Figure 2. Example of a CH$_4$ concentration enhancement (ΔXCH$_4$) map derived from a PRISMA ~~data set~~ dataset that covers an area of coal mines in the Shanxi region (China). The only detected plume is ~~marked~~ pointed out with a red arrow and is originated from a venting shaft. The retrieval is derived from a matched filter formulation using the 2100-2450 nm CH$_4$ absorption window. The true color image source is © Google Earth.

2 Materials and ~~Methods~~methods

2.1 Matched filter for CH$_4$ enhancement concentration mapping

If radiation arrives at the detector without CH$_4$ absorption from an emission ($\cancel{L_0}\mathbf{L_{NoAbs}}$) and also with CH$_4$ absorption

80 ($\cancel{L}\mathbf{L_{Abs}}$), according to the Beer-Lambert's law, $\cancel{L}$ the radiance spectrum $\mathbf{L_{Abs}}$ will be characterized by

$$\cancel{L}\mathbf{L_{Abs}} = L_0\mathbf{L_{NoAbs}} \cdot e^{\alpha k(\Delta\text{XCH}_4 \cdot \mathbf{K_{CH_4}})} \tag{1}$$

where $\cancel{\alpha}$ ΔXCH$_4$ is the CH$_4$ column concentration enhancement in ~~parts-per-billion (ppb), and k~~ ppb, and $\mathbf{K_{CH_4}}$ is the CH$_4$ unit absorption spectrum, which characterizes CH$_4$ absorption features. Note that ~~the CH$_4$ concentration enhancement can also be symbolized by ΔXCH$_4$. k~~ bold font is used to denote vectors. Moreover, $\mathbf{K_{CH_4}}$ is calculated using a LookUp

85 Table adapted to the angular configuration of the scene ~~and deduced from the~~ that relates CH$_4$ transmittance spectra from the ~~HITRAN~~MODTRAN ~~absorption database (?). Note that HITRAN does not consider scattering, but we can ignore it because it is not relevant in the~~ (Spectral Sciencies, Inc., 2016) radiative transfer code to CH$_4$ column concentration values. We do not consider atmospheric scattering in the calculation of transmittance for the SWIR ~~(?)~~spectral range, assuming a

pristine atmosphere. Nevertheless, in certain cases such as in the presence of dust particles or in dark surfaces with low solar zenith angles, the influence of scattering can be significant (Thorpe et al., 2014). Note that $\mathbf{K_{CH_4}}$ in satellite-based missions is calculated considering the integration of CH_4 over an 8 km high column such as in Thompson et al. (2016), while in airborne missions is calculated over the specific flight height. Then, the exponential of the Eq. 1 can be expanded as a Taylor series of infinite terms, and it can be simplified to the second term if we assume a sufficiently small argument of the exponential. This implies that the approximation will generate more accurate results for lower ΔXCH_4. Then, assuming this simplification, radiance can be approximated to a linear function of ΔXCH_4, which will be used for the matched filter method.

The matched filter models a scene radiance data cube as a multivariate Gaussian, where each spectral band is considered to follow a Gaussian distribution. The spectral mean vector ($\boldsymbol{\mu}$) and the covariance matrix (Σ) are retrieved from the data cube and characterize the whole image, while assuming enough homogeneity and CH_4 emission sparsity through the scene. Then, the radiance spectrum of each pixel ($\mathbf{L}$) can be assessed following two different hypotheses. The null hypothesis (H_0), where radiance is simply assessed as background radiance, and the alternative hypothesis (H_1), where it is assessed as the background radiance plus a term that represents CH_4 absorption (Thompson et al., 2016). These hypothesis are represented as follows

$$H_0 : \mathbf{L} \sim \mathcal{N}(\boldsymbol{\mu},\, \Sigma) \tag{2}$$

$$H_1 : \mathbf{L} \sim \mathcal{N}(\boldsymbol{\mu} + \Delta XCH_4 \cdot \mathbf{t},\, \Sigma) \;=\; \mathcal{N}(\boldsymbol{\mu}(1 + \Delta XCH_4 \cdot \mathbf{K_{CH_4}}), \Sigma) \tag{3}$$

where $\mathcal{N}$ represents a multivariate Gaussian distribution with the mean vector and covariance matrix located in its first and second arguments, respectively. The CH_4 absorption term from H_1 is given by the linear term $\Delta XCH_4 \cdot \mathbf{t}$, that comes from linearizing the exponential function from Eq. 1. $\mathbf{t}$ is the target signature that spectrally characterizes the absorption of CH_4 per unit of concentration and is obtained by an element-wise multiplication between the $\boldsymbol{\mu}$ and the $\mathbf{K_{CH_4}}$ arrays, where $\mathbf{K_{CH_4}}$ is first convolved to the instrument's spectral response.

In order to obtain the ΔXCH_4 values, the probability of H_1 occurring is maximized following the maximum likelihood estimation (Eismann, 2012). As a result, we obtain this expression

$$\Delta XCH_4 = \frac{(\mathbf{L} - \boldsymbol{\mu})^T \Sigma^{-1} \mathbf{t}}{\mathbf{t}^T \Sigma^{-1} \mathbf{t}} \tag{4}$$

Datasets used in this study come from push-broom imaging spectrometer missions (AVIRIS-NG, EnMAP, and PRISMA) that scan the swath of the scene with a 2-D detector array. Differences in central wavelength and spectral resolution can exist among detectors from the same array because of optical aberrations (Guanter et al.,

2009), which compromises the uniformity between the data cube columns in the ~~across track~~ across-track direction. Therefore, the matched filter is applied ~~in a per-column basis~~for each along-track column separately.

120   Along the SWIR spectral window there are two CH_4 absorption windows, namely a weaker one around 1700 nm and a stronger one around 2300 nm. The 2300 nm window (roughly 2100-2450 nm) is typically chosen for CH_4 ~~(Thompson et al., 2015; Guanter~~ mapping (Thompson et al., 2015; Foote et al., 2020; Guanter et al., 2021; Irakulis-Loitxate et al., 2021) because the more intense absorption and spectral sampling allows to better characterize CH_4 in comparison to the other window. Hereinafter we will refer this spectral range selection as 2300-MF. There are usually elements from the scene such as roads, solar panels, and

125   buildings that present absorption features similar to CH_4 in the 2300 nm window. Therefore, we will find retrieval artifacts, i.e., pixels with positive ΔXCH_4 values related to these structures. Retrieval artifacts usually present higher ΔXCH_4 values than background noise and can disturb CH_4 plume detection. In fact, they ~~difficult~~ complicate the identification of the real plumes and can even lead to false positives. ~~In this work, we reduce the presence or the intensity of retrieval artifacts by expanding~~ Now, we examine the functionality of the matched filter ~~spectral range of application to the whole SWIR (1000 − 2500 nm).~~

130   ~~Hereinafter we will call this spectral range selection as SWIR-MF. In this spectral range, apart from also accounting for the 1700 nm window, we account for~~ to minimize the presence of retrieval artifacts.

    In Figure 3, we show a scatter plot between two spectral bands with ~~practically~~ CH_4 absorption (2371 nm) and with no CH_4 absorption ~~. Retrieval artifacts coming from similar features in the 2300 nm window can present other different features along the SWIR where CH~~(2102 nm) from a PRISMA dataset covering a homogeneous arid area in Sudan. The ΔXCH_4 ~~does~~

135   ~~not absorb. This should lead to a greater capability to discriminate between the true CH~~values resulting from applying the matched filter using only these two bands are illustrated following the color gradient on the right side of the figure. Note that the radiance data points are plotted relative to the mean values, highlighting the impact of shifts from these central values in the retrieved data. A linear fit based on these shifts allows us to determine the lines equivalent to the ΔXCH_4 ~~emissions and retrieval artifacts.~~

140   ~~According to Eismann (2012), given a N-dimensional space in which each dimension is referred to each spectral band,~~ values of -1, 0, and 1 parts-per-million (ppm). Moreover, three pixels from the original dataset were selected and transformed to represent different situations: one with a 1 ppm natural absorption, another with a 1 ppm absorption according to the matched filter ~~direction is determined through a balance between the minimum background variance direction and the reference spectrum direction~~$(\mu + \alpha \mathbf{t})$. ~~The matched filter direction defines the regions in the N-dimensional space where CH~~model, and

145   a third to illustrate the presence of a retrieval artifact. The absorption based on the model aligns with the alternative hypothesis H_1 from Eq. 3, indicating a deviation from the mean radiance spectrum in the target spectrum direction. Instead, the natural absorption, which reflects a realistic CH_4 ~~emission related pixels should be found. We can observe this in the top panel from Figure ??, where an scatter plot from a matched filter that used only 2 bands from a EnMAP data set from a site in an O&G field in Turkmenistan is illustrated. One band is located at 2191 nm, where there is barely~~ absorption, is implemented by deviating

150   the radiance spectrum of a randomly chosen pixel in the dataset also in the target spectrum direction. On the other hand, the
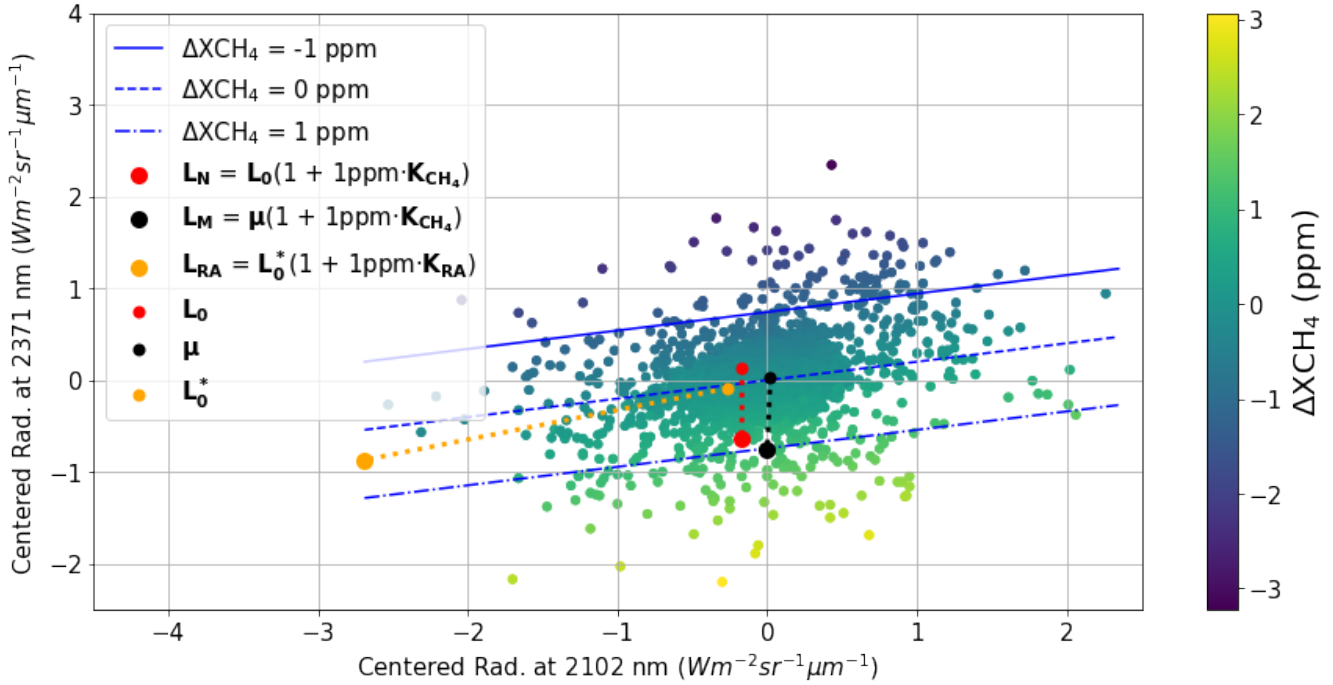
Figure 3. Scatter plot between the centered radiance data points from the spectral band with no CH_4 absorption (2102 nm) and with CH_4 absorption (2371 nm) from a PRISMA dataset. The corresponding ΔXCH_4 values result from the matched filter applied to the two spectral bands and are plotted following the colorbar at the right. The blue lines indicate the domain in where the data points have ΔXCH_4 values of -1 (top), 0 (center) and 1 (bottom) parts-per-million. Small dots from the legend are the original data points before the effective absorption of 1 ppm (big dots) for the natural (red), modeled (black) and the retrieval artifact (orange) cases.

retrieval artifact was generated similarly to the natural absorption case but with an additional deviation in the non-absorption band, where the target spectrum has a null value. The radiance spectra related to these three cases are expressed as follows:

$$\mathbf{L_N} = \mathbf{L_0}(1 + 1ppm \cdot \mathbf{K_{CH_4}}) \tag{5}$$

155 $$\mathbf{L_M} = \boldsymbol{\mu}(1 + 1ppm \cdot \mathbf{K_{CH_4}}) \tag{6}$$

$$\mathbf{L_{RA}} = \mathbf{L_0^*}(1 + 1ppm \cdot \mathbf{K_{RA}}) \tag{7}$$
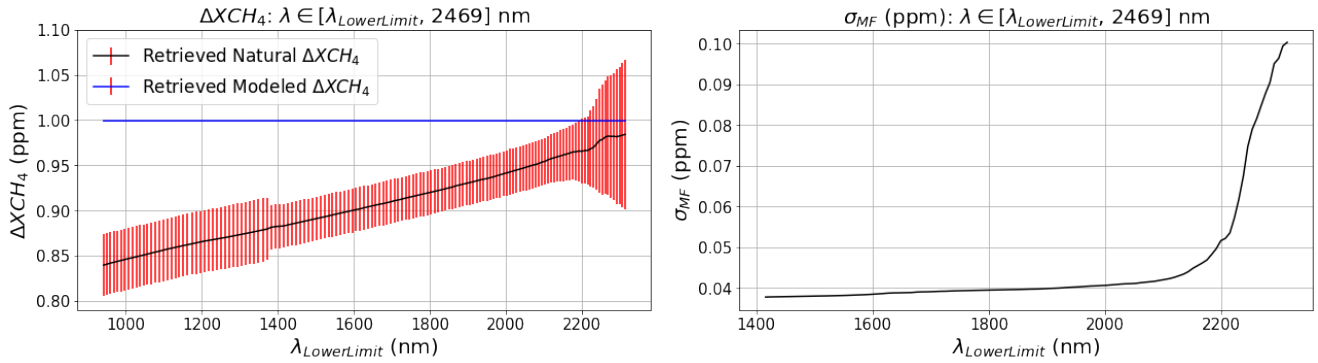
Figure 4. In the left panel, the mean ΔXCH_4 values related to the retrieved natural (black) and modeled (blue) artificial absorptions applied to 1000 different pixels from a PRISMA dataset and their associated error bars (red). In the right panel, a standard deviation σ_{MF} resulting from the Gaussian distribution that is followed by the dataset retrieved values. The matched filter spectral range of application ranges from a variable wavelength value ($\lambda_{LowerLimit}$) to 2469 nm.

where $\mathbf{L_N}$, $\mathbf{L_M}$, and $\mathbf{L_{RA}}$ are the radiance spectra vectors referring to a 1 ppm natural absorption, a 1 ppm modeled absorption, and a retrieval artifact, respectively. $\mathbf{L_0}$ and $\mathbf{L_0^*}$ are the selected radiance spectra vectors from the original dataset pixels, and $\mathbf{K_{RA}}$ is a made up equivalent unit absorption spectrum for the retrieval artifact. The difference between $\mathbf{K_{RA}}$ and $\mathbf{K_{CH_4}}$ is that $\mathbf{K_{RA}}$ presents a non-zero value in the band with no CH$_4$ absorption, ~~while the other one shows a prominent absorption in 2369 nm. We can observe that values that more strictly follow the matched filter direction have greater α values, which are generally related~~. While the modeled absorption in $\mathbf{L_M}$ results in 1 ppm, the natural absorption in $\mathbf{L_N}$ suffers from underestimation due to the deviation of the original pixel radiance $\mathbf{L_0}$ from the mean. Different original values, characterized by diverse deviations, could have also led to overestimated ΔXCH_4 values. Therefore, deviations from the model will probably introduce biases in the retrieved values. Note that in Figure 3, the retrieval is expected to yield a wide range of ΔXCH_4 values due to the limited number of bands involved. On the other hand, while the retrieval artifact $\mathbf{L_{RA}}$ exhibits a spectral feature similar to CH$_4$ ~~emission pixels. When opening~~ in the absorption band, it also displays a characteristic deviation in the non-absorption band that enables better discrimination from CH$_4$. Thus, by expanding the spectral window ~~to the whole SWIR spectrum the reference spectrum to match is more demanding, which would attenuate or remove retrieval artifacts because spectral features beyond the 2300 nm window~~ penalize them.

~~Scatter plots showing the comparison between the 2191 nm (top)/ 902 nm (bottom) no absorption bands and the 2369 nm absorption band. Data points are colored according to where they are located in the Gaussian distribution based on the matched filter retrieval derived from an EnMAP data set showing an O&G field located in Turkmenistan with CH$_4$ emissions. The top panel also shows the matched filter threshold lines and the matched filter direction.~~ in the matched filter application, a more comprehensive discrimination between retrieval artifacts and CH$_4$ may lead to their attenuation or complete removal.

~~Although~~ Additional variations may arise by expanding the window, as depicted in Figure 4. For 1000 different pixels from the already employed ~~SWIR-MF~~PRISMA ~~reduces retrieval artifacts with respect to 2300-MF, there are some limitations when using it. New retrieval artifacts can appear because we are including the 1700 nm~~ dataset, absorptions of 1 ppm were applied using modeled and natural absorptions with Eq.6 and Eq.5, respectively. In the right panel, we show the standard deviation resulting from the entire matched filter retrieval values when using a spectral window comprising a variable lower limit ($\lambda_{LowerLimit}$) and 2469 nm. We select this upper limit because it allows to cover the entire 2300 nm CH_4 absorption window. ~~However, they are attenuated in the same manner as those from the 2300 nm window. In addition, due to the use of a wide spectral window, another limitation comes from including spectrally distant bands, which present a higher degree of decorrelation. We can see this in the bottom panel from Figure ??, where we find a similar scatter plot to the one at the top panel but changing the no absorption band to another one that is spectrally more distant at 902 nm. In comparison to the previous scatter plot, we can observe that data points are more scattered than in~~ Incorporating more bands implies a more demanding spectrum-to-match, and the covariance matrix will better suppress the background, which will result in a lower standard deviation in the retrieval. In the ~~first plot. Additionally, in Figure ?? a correlation matrix from this data set is illustrated and shows us that distant bands (upper-right and lower-left corners) have lower correlation, which leads to a lower weight of the background variance direction. This difficults the discrimination between plume pixels and background pixels, which can lead to enhanced background clutter and plume pixel attenuation. Note that there are bands with very low correlation because of the strong H_2O and CO_2 absorption . We remove these bands from the SWIR-MF in order to not account for their negative impact~~left panel, we display the mean ΔXCH_4 values retrieved from the pixels with the modeled (blue) and natural (black) absorptions, along with their related standard deviation values (red) as a measure of uncertainty. While modeled absorption consistently retrieves the expected 1 ppm value with negligible uncertainty, natural absorption yields progressively lower values when expanding the window. Similar to the background pixels, the accumulated deviations from the natural absorption compared to the modeled absorption will result in a reduction of the retrieved enhancement. As we can see, incorporating more bands make the matched filter more sensitive to spectrum changes, which could lead to a background noise reduction and an underestimation of the ΔXCH_4 values from plume pixels. This increased sensitivity could also capture undesired variations from the modeled spectrum due to factors unrelated to methane, such as atypical albedo values or instrument noise, potentially resulting in clutter noise. Moreover, new retrieval artifacts may appear when including the 1700 nm absorption window, although they would be attenuated in the same manner as those from the 2300 nm window.

~~Correlation matrix of the SWIR spectral bands from a data set showing an O&G field located in Turkmenistan with CH_4 emissions. Note that the axes reflect the wavelength values in nm of the spectral bands.~~

We have not considered yet ~~interferences with other traces~~ the interference with other trace gases such as the H_2O and CO_2 ~~on the not removed bands~~ when expanding the window (see Figure 1). Absorption features from these gases appear along the SWIR spectral region and might ~~disturb CH~~cause further biases on the ΔXCH_4 ~~retrieval values. Generally,~~ values from plume pixels. The left panel of Figure 4 shows a sudden increase of the standard deviation of the retrieved ΔXCH_4 values related to the natural absorption when including several spectral bands around 1400 nm. This occurs because an important fraction of radiance pixels in these bands contains absolute zero values due to strong H_2O absorption, which violates the assumption of

Gaussian modeling in the matched filter. Consequently, we exclude these bands along with those associated with the strong H_2O absorption around 1900 nm, as they may also compromise the retrieval due to their very low values. Moreover, the atmospheric concentrations of H_2O and CO_2 ~~atmospheric concentrations~~ are approximately homogeneous across the area captured in one ~~data set~~dataset. However, ~~atmospheric concentration variations~~ variations in atmospheric concentration of H_2O are given when there are pronounced height variations of the terrain across the scene (Lou et al., 2021). ~~Thus, unless the data set~~ Unless the dataset area meets this condition, we can assume homogeneity. As a result, variations from the mean array ~~could not be related~~ cannot be attributed to these gases, which implies that the matched filter should not be affected by them. Nevertheless, ~~there are cases of coemission of CH₄ and~~ the coemission or overlapping of plumes from H_2O or CO_2 ~~plumes such as in~~ with CH_4 plumes has not been studied yet. Simulations will be employed to understand how they impact the retrieval. This could help to understand methane concentration maps in situations such as inefficient flaring (Irakulis-Loitxate et al., 2021)~~. In these cases, the CO₂~~, where there is coemission of CH_4 and CO_2 ~~presence would disturb the~~ plumes.

2.2 Combo-MF

In this work, we propose to expand the matched filter spectral range of application to the whole SWIR (1000 – 2500 nm) in order to remove retrieval artifacts and therefore to improve CH_4 ~~detection because the radiance spectra from these pixels would be deviated from the reference spectrum, which should result in a lower enhancement~~plume detection. Hereinafter we will call this spectral range selection as SWIR-MF. This selection would be unfeasible using physically-based methods such as the IMAP-DOAS (Frankenberg et al., 2005) because of the growing complexity of separating atmospheric absorptions from surface spectral features (Thorpe et al., 2014). Also note that the increased number of spectral bands does not substantially impact the computational processing time required when applying the matched filter.

~~Then, with~~ As we observed in Figure 4, SWIR-MF ~~we will obtain greater enhancement values coming from 1700 nm retrieval artifacts and clutter, while there will be lower enhancement from 2300 nm retrieval~~artifacts and plume pixels. ~~Even lower enhancements will be found in the case of CO₂ and CH₄ plume overlapping~~produces overall smaller ΔXCH_4 values than 2300-MF. This is especially true for those retrieval artifacts that are displayed in the 2300-MF retrieval. However, expanding the window could also derive in the appearance of clutter due to the higher matched filter sensitivity and the inclusion of new absorbing bands that could lead to the emergence of new retrieval artifacts. Therefore, SWIR-MF values greater than the ~~2300-MF values~~ 2300-MF values will probably come from disturbing factors. ~~Most of the pixels meeting this condition belonged to the negative part of the normal distribution of the 2300-MF values because they were not considered as CH₄ in this spectral window, but with SWIR-MF they are converted into positive due to 1700 nm retrieval artifacts and the emergence of new clutter noise.~~ As a solution, we change these values to the ones of the original 2300-MF in order to penalize the increased enhancement. ~~This generates a greater contrast between the emission and its surroundings because a great fraction of the transformed values present negative values.~~ On the other hand, to solve the underestimation from plume pixels and ~~make~~

~~values comparable to the 2300-MF values~~keep the variances of both retrievals comparable, we multiply the remaining retrieval values by a factor f defined as

$$f = \frac{\sigma_{\text{2300-MF}}}{\sigma_{\text{SWIR-MF}}} \frac{\sigma_{(2300)}}{\sigma_{(SWIR)}} \tag{8}$$

where ~~$\sigma_{\text{2300-MF}}$ and $\sigma_{\text{SWIR-MF}}$~~ $\sigma_{(2300)}$ and $\sigma_{(SWIR)}$ are the standard deviations from the ~~retrievals~~ Gaussian distributions that are followed by the ΔXCH_4 retrieved values from the dataset resulting from applying the 2300-MF and ~~the~~ SWIR-MF retrievals, respectively. ~~Retrievals~~ Generally, retrievals follow a normal distribution with an averaged value of ~ 0, so we can scale the distribution of not-transformed SWIR-MF values to the one of the ~~the~~ 2300-MF values by simply multiplying by f. Then, the transformed values from the SWIR-MF retrieval will follow approximately the 2300-MF retrieval normal distribution. In this manner, plume pixel values will be approximately scaled to the enhancement levels from the 2300-MF retrieval in order to solve the underestimation. ~~Note that we~~ We will call this procedure ~~as~~ Combo-MF~~and a flow chart depicting how it is obtained is illustrated in Figure ??~~, which can be expressed as

$$\Delta XCH_{4(Combo)} = \begin{cases} f \cdot \Delta XCH_{4(SWIR)} & \text{if } \Delta XCH_{4(SWIR)} < \Delta XCH_{4(2300)} \\ \Delta XCH_{4(2300)} & \text{if } \Delta XCH_{4(SWIR)} \geq \Delta XCH_{4(2300)} \end{cases} \tag{9}$$

where $\Delta XCH_{4(2300)}$, $\Delta XCH_{4(SWIR)}$, and $\Delta XCH_{4(Combo)}$ are the CH_4 column enhancement values from the 2300-MF, SWIR-MF, and Combo-MF retrievals, respectively. As a result, limitations from the SWIR-MF are mitigated: ~~disturbing 1700 nm retrieval artifacts and~~ the emergence of new clutter noise ~~are~~ is removed, and the SWIR-MF values are transformed into typical 2300-MF value levels. ~~In~~ Nevertheless, in pixels where surface structures related to a retrieval artifact are positioned beneath a CH_4 emission, there might be a more pronounced attenuation that could compromise the detection. Moreover, in Figure 5 we can see retrieval histograms from ~~a~~ an EnMAP ~~data set~~ dataset from an O&G field in Turkmenistan when applying 2300-MF, SWIR-MF, and Combo-MF. We can observe that SWIR-MF has a lower standard deviation because of a more stringent spectrum that ~~penalizes retrieval artifacts and underestimates plume ΔXCH_4~~reduces background noise. The Combo-MF takes a standard deviation close to the one from the 2300-MF because of the scaled values, but its mean is shifted to negative values because a great fraction of the 2300-MF values from Combo-MF are negative. Therefore, there is a lower amount of pixels with positive ~~enhancent~~enhancement, which implies a better contrast between plume pixels and their background. ~~Note that pixels with overlapped CO_2 and CH_4 plumes would still suffer from underestimation, which can be relevant depending on how concentrated is the CO_2 plume.~~

~~Diagram describing how Combo-MF is carried out from the SWIR-MF and 2300-MF values.~~

Combo-MF is not the unique alternative created to improve CH_4 emission detection. Instead, there exist other matched filter derived methods such as the *Matched filter with Albedo correction and reweighted L1 sparsity code* (MAG1C) that has been used in some studies ~~(Foote et al., 2021; Knapp et al., 2023; Ayasse et al., 2022)~~(Foote et al., 2021; Ayasse et al., 2022; Knapp et al., 2023
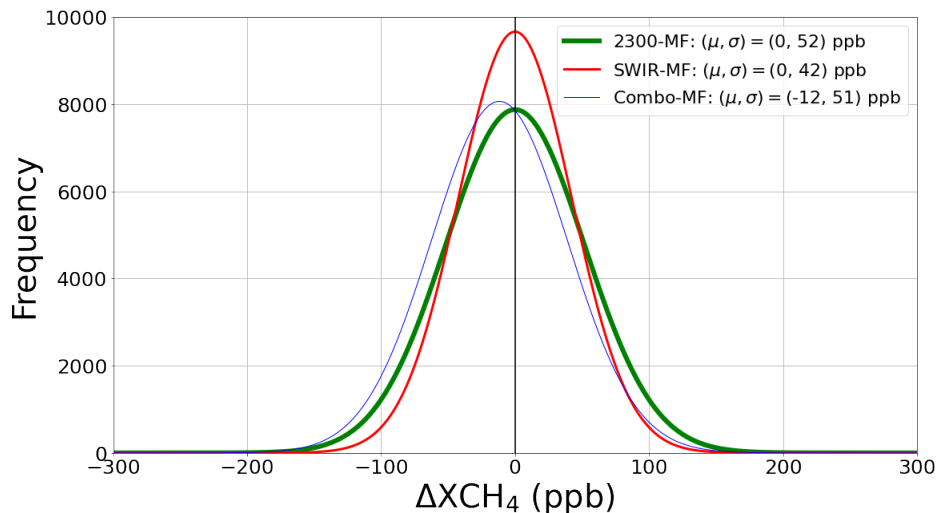
Figure 5. Histrogram from ~~2300-MF~~ 2300-MF (green), ~~SWIR-MF~~ SWIR-MF (red), and ~~Combo-MF~~ Combo-MF (blue) retrieval histograms from an EnMAP ~~data set~~ dataset showing a O&G field located in Turkmenistan with CH_4 emissions. μ and σ are the mean and standard deviation values from the different distributions, respectively.

. It applies an albedo correction across the radiance data cube in order to account for the homogeneity assumption from the matched filter. In addition, MAG1C leverages the CH_4 sparsity assumption and also applies an iterative regularization that aims to reduce background noise. MAG1C retrievals values can be divided in two groups: 1) zero-values that were obtained because of the sparsity assumption and 2) a set of values that follow a log-normal distribution and mostly refer to retrieval artifacts and CH_4 emissions. If we transform the retrieval in order to follow a normal distribution, the resulting standard deviation will not be related to the random background noise, as happens with Combo-MF, and therefore we will not be able to compensate a potential underestimation when extending the spectral window. Because of this reason, we will not apply an equivalent Combo-MF methodology to MAG1C. Thus, we will compare MAG1C retrievals using the 2300 nm absorption window (2300-MAG1C) and the whole SWIR spectral region (SWIR-MAG1C) to the Combo-MF retrievals in order to assess if the latter improves plume detection.

2.3 Simulated trace gas enhancements

ΔXCH_4 maps depicting simulated plumes with different shapes, related wind speed values, and concentrations have been generated using large-eddy simulations with the Weather and Research Forecasting Model (WRF-LES) (Varon et al., 2018; Cusworth et al., 2019). Using the deduced LookUp Table used to obtain $\mathbf{K_{CH_4}}$, the ΔXCH_4 values associated with the synthetic plumes are transformed into their equivalent transmittance spectra. Then, transmittance is convolved to the instrument's spectral response and multiplied by the original radiance dataset, accounting for minor radiometric offsets (Guanter et al., 2021). These

plumes are implemented in three different ~~data sets~~ datasets from the PRISMA mission to assess the CH_4 emission detection and quantification capabilities from the different procedures.

290   ~~In addition, simulated enhancements from~~ Simulations are also used to assess the impact of H_2O and CO_2 ~~have been implemented homogeneously across the whole area extent from a PRISMA data set. Specifically, typical background enhancements of~~ on the retrievals. Simulated enhancements of typical background concentrations for CO_2 (2500–10000 ppb ~~for CO_2 (C3S, 2018) and of~~) (C3S, 2018) and H_2O (1–2.5 g/cm^2 ~~for H_2O (Mieruch et al., 2014) were implemented homogeneously across this data set in order to study how~~) (Mieruch et al., 2014) are uniformly applied to the whole extent of a PRISMA dataset with a constant

295 value. This allows us to examine how variations in the atmospheric concentrations of these trace gases ~~would~~ affect CH_4 retrievals ~~when~~ using 2300-MF and ~~SWIR-MF~~Combo-MF. ~~In this manner, we can test whether a greater or lower background concentrations of these two trace gases have an impact in~~ Additionally, we introduce H_2O and CO_2 enhancements exclusively on pixels where we implemented a simulated CH_4 plume to assess the impact of these trace gases on the plume ΔXCH_4 values in the case of coemission or overlapping plumes. A constant enhancement of 10 ppm has been applied for CO_2, and 100 ppm

300 for H_2O, considering the order of magnitude observed in some CO_2 and H_2O plumes reported by Cusworth et al. (2023) and Thorpe et al. (2017), respectively.

2.4   Detection and quantification of point-source emissions

Generally, the detection of CH_4 ~~retrieval. However, because of~~ plumes is performed through a supervised methodology, which involves a direct visual inspection of the retrieval. First, we search for clusters with plume-like shapes and with ΔXCH_4 values

305 greater than background noise values. Then, we validate the association with a potential CH_4 source using high-resolution images from Google Earth data or the spectral radiance bands within the dataset. Finally, we confirm the cluster as a true plume by validating its alignment with the wind direction, which can be retrieved from the GEOS-FP database (Molod et al., 2012). For instance, the emission in Figure 2 was confirmed as the only plume in the image according to these steps. However, in order to establish a systematic procedure to study the detection capabilities of both the 2300-MF and Combo-MF, we will use

310 an automatic detection algorithm instead of the ~~homogeneity of these enhancements across the scene there should not be any~~ supervised initial selection of clusters associated with potential plumes. The algorithm begins by applying a 3 x 3 median filter to the retrieval to mitigate the impact of random noise in the classification process (Varon et al., 2018). Subsequently, a mask is generated, retaining only those values from the filtered retrieval that exceed 1 standard deviation from the ~~mean value that could be related to them. Therefore, this enhancements should not disturb retrieval values~~Gaussian distribution followed by the

315 originally retrieved values. It is assumed that this threshold is reasonable for effectively distinguishing between background and plume pixels (Guanter et al., 2021). Next, a filter based on morphological parameters is applied to the resulting mask, isolating clusters with plume-like shapes. Finally, an analysis following the remaining supervised detection steps is applied to the persisting clusters, keeping only those related to CH_4 plumes.

2.5   ~~Quantification of point-source emissions~~

320 ~~The~~ On the other hand, the parameter typically used to quantify the intensity of ~~a~~ CH$_4$ ~~emission~~ emissions released from a point-source is the flux rate (Q in $\mathrm{kg/h}$). As in Varon et al. (2018), we can express this magnitude as

$$Q = \frac{U_{\mathrm{eff}} \cdot \mathrm{IME}}{L} \tag{10}$$

where U_{eff} (m/s) is the effective wind speed, a parameter that linearly depends on the wind speed at 10 m above the surface (U_{10}) ~~that is given as an output from the~~ for ~~WRF-LES~~ PRISMA ~~simulations~~ and EnMAP data (Guanter et al., 2021; Roger et al., 2023)

325 , L (m) is obtained as the square root of the plume mask area, and IME (kg) is the mass related to the CH$_4$ enhancement contained in the masked plume (Frankenberg et al., 2016). IME and L depend on the plume mask, which makes masking an important factor that impacts on the accuracy of quantification. Masking is ~~done by the following steps:~~

~~A median filter is applied to the retrieval to remove high-frequency variations related to background noise . We create a mask that only filters those values from the resulting median filter retrieval that are greater than 1 standard deviation from~~

330 ~~the retrieval. We use 1 standard deviation because it is the value at which we consider that we can detect the plume by visual inspection (Guanter et al., 2021). Note that for the~~ performed with the automatic algorithm used for detection. The resulting masks from both 2300-MF and Combo-MF retrievals may differ due to variations in background noise and the presence of retrieval artifacts. Moreover, the ΔXCH$_4$ values of Combo-MF plume pixels cannot be trusted for quantification because the factor f used is only valid for scaling to typical ~~Combo-MF~~ 2300-MF ~~we use the standard deviation of the~~ values, and it does

335 not ensure the accuracy of the enhancement values. To assess whether the masking from Combo-MF improves quantification compared to 2300-MF ~~retrieval because its values are scaled to 2300-MF values. We select the overlapped pixels from two masks. One is the resulting mask from the previous step and the other one delimits~~ , we will implement a quantification strategy using Combo-MF masking and 2300-MF values, which we call Mix-MF. This comparison is performed on multiple simulated plumes with known Q and U_{eff} values that have been applied to real datasets. A preliminary mask, delineating the

340 plume shape coming directly from the simulation ~~. This is done because we only want to keep those pixels related to the plume area.~~

~~Combo-MF retrievals present a lower background noise at positive values, which makes it easier to isolate the plume from its sorroundings. This should positively affect masking, although values transformed by a simple factor in the Combo-MF retrieval should not be trusted for quantification. Thus, we will compare the quantification based exclusively on the 2300-MF and, the~~

345 ~~quantification based on 2300-MF values and Combo-MF masking. This quantification strategy that mix both retrievals will be called Mix-MF~~ data, is implemented to eliminate the influence of retrieval artifacts, which allows the isolation of background noise as the only disturbing contribution to quantification. This is also done to automatize the quantification process due to the large number of simulated plumes used for this analysis.

2.5 Imaging spectroscopy data

350 In this work, we have used Top-of-Atmosphere radiance ~~data sets~~ datasets from the PRISMA, ~~GF5-02 AHSI,~~ EnMAP, and AVIRIS-NG missions. ~~In order to implement simulated trace gases enhancements we have chosen~~ A PRISMA ~~samples from~~

Table 1. ~~Mission, location, sector where the CH~~$_4$~~ emission was originated, date, and central coordinates from~~ Information about the ~~data sets~~ datasets used in this study. They are listed in order of appearance in this work. Dates are in YYYY-MM-DD format, and latitude and longitude coordinates (*Lat/Lon*) are in decimal degrees.

Mission	Location	Sector	Date	Lat/Lon
PRISMA	Shanxi (China)	Coal mining	2020-04-28	37.831/113.701
PRISMA	Northern State (Sudan)	Not related to CH$_4$	2020-04-01	21.900/28.000
EnMAP	Ekizak (Turkmenistan)	O&G	2022-10-02	38.685/54.243
PRISMA	Silesia (Poland)	Coal mining	2022-03-02	50.110/17.895
PRISMA	In Amenas (Algeria)	O&G	2021-01-15	28.286/9.638
PRISMA	Permian Basin (U.S.)	O&G	2020-06-30	31.437/-103.480
~~GF5-02 AHSI Permian Basin (U.S.) O&G 2022-02-09 32.798/-104.124~~ AVIRIS NG	San Joaquin Valley (U.S.)	O&G	2017-09-06	35.279/-119.476
EnMAP	Delhi (India)	Landfills	2023-04-24	28.620/77.200
PRISMA	Shanxi (China)	Coal mining	2021-02-06	36.241/112.909

~~a desertic~~ dataset from a coal mining region in Shanxi (China) is selected to exemplify the difficulties in emission detection in CH$_4$ retrievals when using 2300-MF (Figure 2). In this case, only one plume could be detected among a high number of retrieval artifacts. Another PRISMA dataset from a Sudan area is used to illustrate how the matched filter scores background,

355   retrieval artifacts, and plume pixels by introducing artificial absorptions and retrieval artifacts (Figure 3). It is also used to assess its performance when expanding the spectral window of application (Figure 4). This dataset shows a very low surface variability and no emissions, simplifying the analyses. Additionally, for implementing simulated enhancements of different trace gases, we selected PRISMA datasets from an arid O&G field in Argelia, an O&G field ~~from~~ in the Permian Basin (U.S.), ~~and~~ a coal mine site in Poland~~(see Figure 6. Additionally, we show retrievals with detected CH~~$_4$~~ plumes also derived from~~

360   ~~PRISMA samples from coal mines in the Shanxi region (China) (Figure 11). We also present a GF5-02 AHSI sample with~~ ~~overlapped CH~~$_4$~~ and CO~~$_2$~~ plumes from the Permian Basin (U.S.) coming from an inefficient flare (Figure ??). Moreover,~~ , and

an EnMAP ~~sample~~ dataset from an O&G field in Turkmenistan~~is chosen to study the matched filter using only two bands, the decorrelation between all the~~. The latter is also used to show the distribution of ΔXCH$_4$ values when using 2300-MF, ~~SWIR~~bands, and to obtain the histograms (shown in SWIR-MF, and Combo-MF retrievals (Figure 5)~~resulting from applying different procedures. From this mission, we also show the retrievals from a data set capturing a Delhi (India) area where there are the Bhalswa, Gazhipur and Okhla landfills (Figure 10). Finally~~. Note that, although some of the datasets with simulated enhancements present real CH$_4$ emissions, the simulated plumes were intentionally implemented to avoid interference with the actual ones. Moreover, an AVIRIS-NG ~~sample~~ dataset from an O&G field in San Joaquin Valley in California (U.S.) showing two plumes is used in order to show the performance of 2300-MF, Combo-MF, 2300-MAG1C and SWIR-MAG1C procedures~~(Figure 9)~~. In addition, we show retrievals from an EnMAP dataset capturing a Delhi (India) area where there is CH$_4$ release originated in the Gazhipur landfill. Finally, we show the detection capabilities of 2300-MF and Combo-MF in another PRISMA dataset from the Shanxi area, where 15 plumes were identified. More information about these ~~data sets~~ datasets can be found in Table 1.

3 Results

3.1 Real data with simulated trace gas enhancements
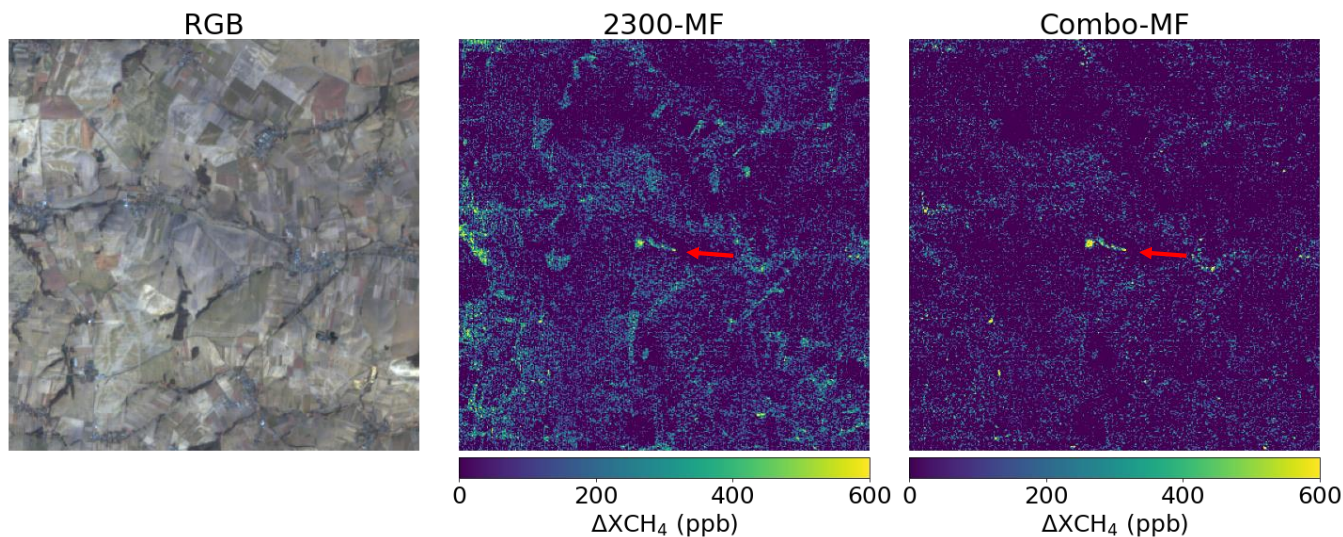
Figure 6. True color image (left), ~~2300-MF~~ 2300-MF retrieval (center), and ~~Combo-MF~~ Combo-MF retrieval (right) from a PRISMA ~~data set~~ dataset from a coal mine site in Poland with an implemented plume with Q = 2000 kg/h. The plume is pointed out with an arrow.

We have implemented simulated CH$_4$ plumes in three PRISMA ~~data sets~~ datasets from three different sites. These areas were selected to study a diverse range of scenarios regarding surface heterogeneity and brightness, which are important factors in the
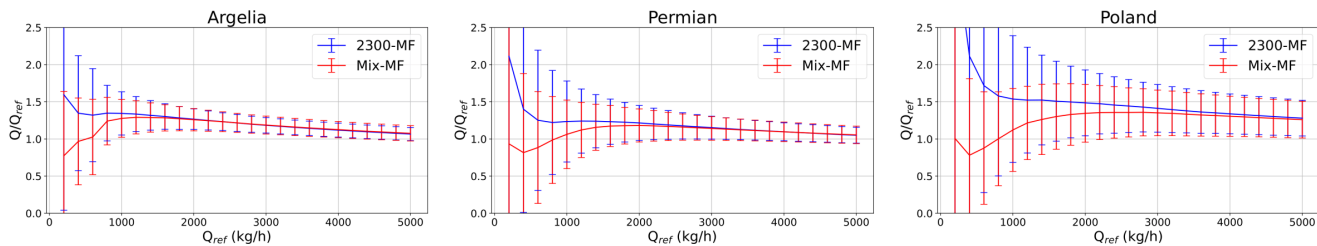
Figure 7. Simulated flux rate Q_{ref} versus the ratio between the deduced flux rate Q and Q_{ref} from 100 different plumes implemented in PRISMA ~~data sets~~ datasets from sites in Argelia (~~top~~left), the Permian Basin (center), and Poland (~~bottom~~right) using the Mix-MF (red) strategy and the 2300-MF retrievals (blue). Plotted points and error bars of each flux rate value correspond to the mean and 1 standard deviation values from the 100 estimates, respectively.

matched filter retrieval. Homogeneous and bright surfaces ~~would~~ will lead to a better performance than more heterogeneous and darker surfaces. The areas selected were an homogeneous and bright ~~desertic~~ arid O&G site from Algeria, an ~~heterogenous~~

380 heterogeneous and bright O&G site from the Permian Basin (U.S.), and an heterogeneous and relatively dark coal mining site in Poland.

In Figure 6 we show ~~an~~ the RGB image and the 2300-MF and Combo-MF retrievals from the Poland site. We can observe a remarkable reduction in the positive background noise values and the attenuation of retrieval artifacts related to the scene topography or to different land covers. As a result, there is a greater contrast between the plume and its surroundings and

385 therefore it is easier to detect the emission by visual inspection. On the other hand, Figure 7 shows the ~~quantification~~ Mix-MF quantification and the one based entirely on the 2300-MF retrieval ~~and the Mix-MF quantification. They are applied in data sets capturing Argelia, Permian Basin, and Poland sites~~. The study ~~was made for~~ covers a flux rate interval ranging from 200 kg/h to 5000 kg/h for 5 different plumes with different shape and ΔXCH_4 distribution. Each one of these plumes was implemented ~~20 times across each data set in different locations~~ in 20 different locations within each dataset and for each flux rate value,

390 i.e., quantification was assessed with 100 plumes for each flux rate value. ~~In this manner, we make the study considering plume and background diversity~~ Thus, we examine the quantification across a diverse range of plumes and backgrounds within the same ~~data set~~ dataset. Error bars ~~showing~~ display 1 standard deviation from the ~~100 plume quantification distribution for each~~ quantification distribution related to each implemented flux rate value ~~are displayed. We find~~ (Q_{ref}). We observe that Argelia and Permian Basin sites present lower uncertainty than the Poland site because the lower brightness from the latter is

395 translated in ~~a lower retrieved signal-to-noise-ratio~~ noisier retrieval. For $Q < 1000$ kg/h, the low ΔXCH_4 plume values, closer to noise level, ~~difficult~~ complicate the masking process. In the 2300-MF quantification case we ~~find~~ observe an overestimation, while for the Mix-MF quantification we ~~find that the more restrictive masking leads to~~ generally obtain more accurate values. The number of pixels with ΔXCH_4 values greater than 1 standard deviation from the distribution followed by the retrieved values are reduced in Mix-MF due to the clutter removal of Combo-MF, resulting in a more restrictive mask that is less

400 affected by background noise. However, for both procedures there is an important uncertainty at these flux rate levels that
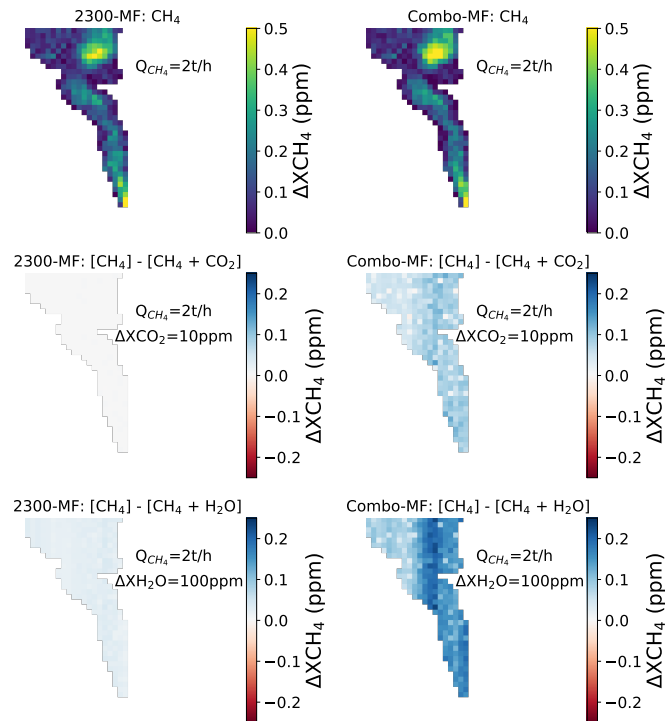
Figure 8. ~~Radiance at 2016 nm~~ Retrieved simulated plume of Q = 2000 kg/h implemented on an EnMAP dataset from a O&G field in Turkmenistan using 2300-MF (left column) ~~, 2300-MF retrieval (center),~~ and ~~Combo-MF retrieval~~ Combo-MF (right column) retrievals (top row), and the difference resulting from applying a ~~GF5-02 AHSI data set from an O&G field in the Permian Basin~~ constant ΔXCO$_2$ value of 10 ppm (~~U.S. centered row~~) ~~showing~~ and a ~~plume~~ constant ΔXH$_2$O value of 100 ppm (~~pointed with an arrow~~bottom row)~~originated from inefficient flaring~~.

limits quantification. For greater Q, there is a progressive uncertainty and overestimation reduction for both procedures that approximates quantification to true values. At these levels, estimations from both quantification strategies align because the greater enhancement from plume pixels lead to a practically identical masking for both of them.

   In addition, typical background enhancements of CO$_2$ and H$_2$O were implemented homogeneously across these three ~~data~~
405 ~~sets~~ datasets in order to assess their impact in 2300-MF and ~~SWIR-MF~~Combo-MF retrievals. As a result, we ~~found~~ observe practically null differences between the enhanced and not enhanced ~~data sets~~ datasets using both procedures. Therefore, this confirms our hypothesis that the atmospheric concentrations of these trace gases do not disturb the retrievals since the changes in radiance are already integrated into the mean value of the scene. On the other hand, we have also studied the influence of CO$_2$ ~~plumes overlapping~~ and H$_2$O enhancements only overlapped with a simulated CH$_4$ ~~plumes in the retrieval when using~~
410 ~~CO$_2$ absorption bands. This overlap can be originated from inefficient flares in~~ plume of Q = 2000 kg/h implemented in an EnMAP dataset covering an O&G ~~fields (Irakulis-Loitxate et al., 2021). One example of this from a GF5-02 AHSI data set is~~

~~illustrated in Figure **??**. At the left panel, we can observe a white dot in the 2016 nm radiance band associated to the flare. Comparing the~~ area in Turkmenistan. In Figure 8, the top row displays the retrieved CH_4 plume obtained using 2300-MF (~~center~~left column) and Combo-MF (right~~) retrievals, we can see that background noise from the latter is reduced, but there is also an attenuation of plume pixel enhancements. Therefore~~column). The centered row shows the difference between the original plume and the same plume with an overlapped constant CO_2 enhancement (ΔXCO_2) of 10 ppm, and the bottom row presents the difference with an overlapped constant H_2O enhancement (ΔXH_2O) of 100 ppm. In the 2300-MF, we can ~~deduce that coexistence with~~ observe that there is a negligible difference when overlapping CO_2 ~~plumes might derive in an underestimation of~~ enhancements because of the little interference in the 2300 nm window. However, this interference does exist for the H_2O case, which results in lower retrieved ΔXCH_4 values. On the other hand, there is an increased underestimation for both trace gases when expanding the window (Combo-MF) because more absorption features that deviate from the CH_4 ~~plume enhancement. Greater underestimation would occur when coemitting with more concentrated~~ absorption spectrum are introduced. Nevertheless, if the bands where other trace gases absorb are discarded when expanding the window, there will be no attenuation in the retrieved values due to the absence of interference with the CH_4 absorption spectrum, as observed in the CO_2 ~~plumes since the approximation to the reference spectrum would be less accurate~~case in the 2300-MF retrieval. Then, when this interference does exist, the degree of underestimation will depend of the overlapped trace gas enhancements levels. Although these enhancements have been applied homogeneously to the plume area, there is an heterogeneous underestimation across the columns that can be more appreciated in the H_2O case. This occurs because the ΔXCH_4 values from the simulated plume and the enhancements from the other traces gases can alter the statistics of the column and therefore resulting in a different underestimation. In addition, the noisy nature from the differences comes mostly from the retrieval noise.

3.2 Real CH_4 plume cases

3.2.1 Comparison to MAG1C retrievals with AVIRIS-NG data

In Figure 9, we compare ΔXCH_4 retrievals using 2300-MF, Combo-MF, 2300-MAG1C, and SWIR-MAG1C from an AVIRIS-NG dataset capturing an O&G field site in San Joaquin Valley (U.S.).~~ We evaluate the performance when widening the spectral window to the whole SWIR spectrum, and assess if there is an improvement in comparison to the Combo-MF performance. The upper limit value selected for representation was different for 2300-MF and Combo-MF retrievals than for 2300-MAG1C and SWIR-MAG1C retrievals. As shown in Guanter et al. (2021), we can find that MAG1C exhibits higher values and therefore a higher upper limit was set to compare retrievals showing approximately the same plume intensity. Therefore, we will be able to assess the contrast between plumes (pointed with arrows) and their surroundings for the different retrievals~~, where two plumes can be observed. 2300-MAG1C retrieval presents ~~a higher~~higher ΔXCH_4 plume values as shown in Guanter et al. (2021) and also exhibits a greater number of retrieval artifacts than 2300-MF. These artifacts are further attenuated or totally removed in the SWIR-MAG1C retrieval. However, SWIR-MAG1C enhances some retrieval artifacts that are not shown when using Combo-MF. The latter ~~leads to a lower background noise in comparison~~presents a lower noise compared to 2300-MF, although it is slightly higher ~~in comparison to~~than in MAG1C~~retrievals because they use the sparstiy assumption~~, which leverages the

445 sparsity assumption for its suppression. Therefore, Combo-MF can be considered as an effective trade-off between reducing background noise and retrieval artifacts. Note that, instead of considering an integration of CH_4 over a 8 km high column ~~for CH_4 integration, we have used~~ as with satellite-based data, we use the scene average sensor altitude ~~obtained from the metadata~~ (2.48 km) from the airborne AVIRIS-NG instrument at acquisition time.
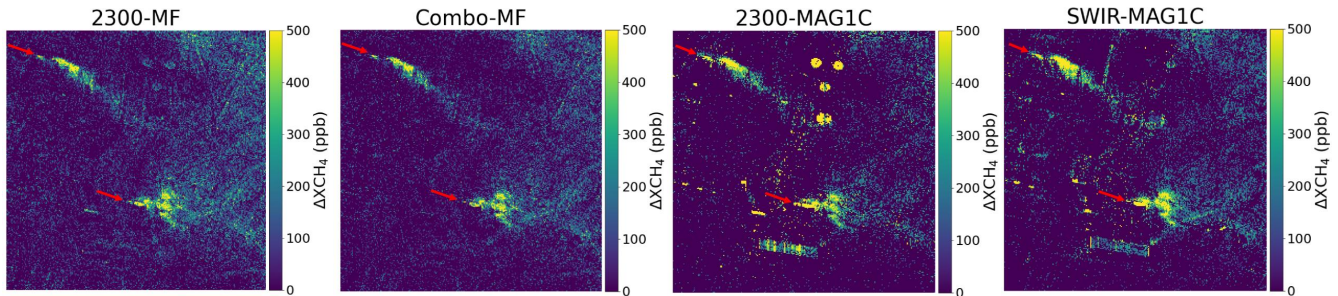
Figure 9. Starting from the left, 2300-MF, Combo-MF, 2300-MAG1C, and SWIR-MAG1C retrievals from an AVIRIS-NG ~~data set~~ dataset showing an O&G field in San Joaquin Valley, California (U.S.). ~~The first two and the last two retrievals were illustrated with a different range of values in order to compare them by visual inspection.~~ Plumes are pointed out with an arrow.

3.2.2 Retrieval performance in a landfill area using EnMAP data

450 ~~Landfill emissions can be detected using EnMAP data (Roger et al., 2023), so we look for some examples using data sets capturing areas with landfills.~~ In Figure 10 ~~we can observe the comparison between~~, the 2300-MF (top-right) and Combo-MF (bottom-right) retrievals from an EnMAP ~~data set from~~ dataset capturing a Delhi area (India) ~~. Here there are located the Bhalswa (top-left), Gazhipur (top-right) and Okhla (bottom) landfills. We can observe the enhancement related to these three landfills (pointed with an arrow) in both retrievals. However, the~~ are compared. Both retrievals show an emission (framed
455 in red) coming from the Gazhipur landfill. While 2300-MF shows a great amount of retrieval artifacts related to the urban area and a higher background noise, ~~while the~~ Combo-MF further attenuates or removes these retrieval artifacts and reduces the positives values from background noise. ~~We can see that the enhancement from the landfills is somewhat attenuated~~ The difference between both retrievals (bottom-left) shows us that there is also attenuation in those pixels where we detect CH_4 emission. In fact, we can appreciate this attenuation in the landfill area in the Combo-MF ~~, which migh be caused because
460 of~~ retrieval. This could be caused by the existence of retrieval artifacts ~~below the emission. Even though, the capability for emission detection~~ beneath the emission, which would penalize the retrieved enhancements when expanding the matched filter spectral window of application. Therefore, an appropriate use of Combo-MF should take into account the surface composition beneath potential methane emissions. Nevertheless, despite this attenuation, the detection capability is remarkably improved. Note that the atmospheric elements that appear in the true-color image (top-left) are mainly related to pollutants following the
465 Mie scattering, which does not substantially affect radiance at SWIR wavelengths (Roger et al., 2023).
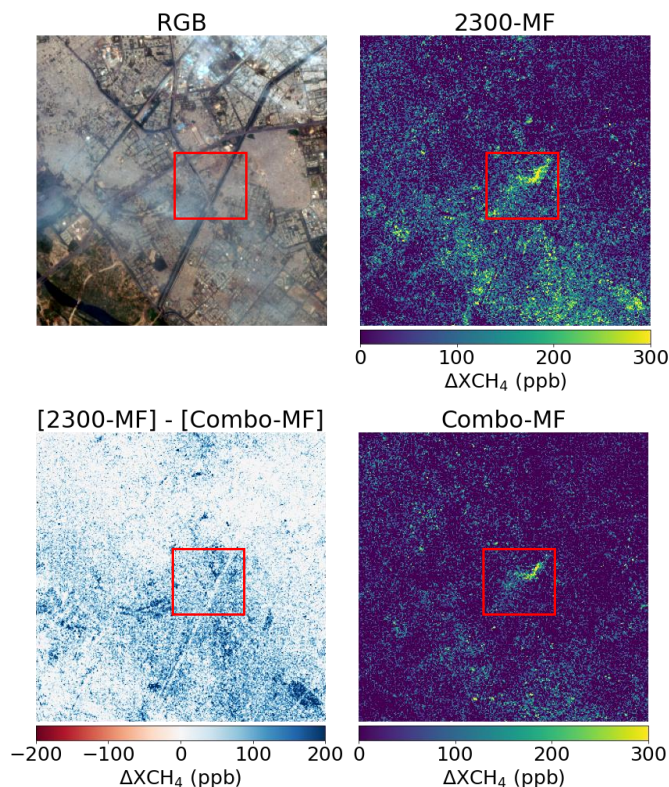
Figure 10. True color image (~~left~~top-left), ~~2300-MF retrieval~~ 2300-MF (~~center~~top-right) and Combo-MF (bottom-right) retrievals, and ~~Combo-MF retrieval~~ the difference between them (~~right~~bottom-left) from an EnMAP ~~data set~~ dataset from Delhi (India) showing an emission from the ~~Bhalswa (top-left),~~ Gazhipur ~~(top-right) and Okhla (bottom)~~ landfill ~~emissions (pointed with an arrow~~framed in red).

3.2.3 Retrieval performance in a coal mining site using PRISMA data

Combo-MF is well-suited for regions with pronounced heterogeneity because there are usually more retrieval artifacts that can be removed. In order to demonstrate this, we ~~do~~ conduct a comprehensive study in a PRISMA ~~data set~~ dataset from a coal mining site in Shanxi (China), which can be considered heterogeneous. ~~First, we identify by visual inspection the CH₄~~

470 ~~emissions with~~ In Figure 11, we illustrate in the central panel 15 plumes detected in the area, which are pointed out with red arrows, over a high-resolution image of the area. These plumes originate from potential emission sources and approximately align with the wind direction, which is extracted from GEOS-FP. Therefore, we validate the existence of these emissions. At the edges of the central panel, we observe four blocks associated with plumes (labeled $a - d$), displayed as an example of the detection process across the scene. In these blocks, we show the zoomed-in view of the emission source (gray) and of the

475 output masks derived from the automatic detection algorithm (see section 2) used in both the 2300-MF ~~retrieval and then we do the same based on the~~ (blue) and Combo-MF ~~retrieval. In Figure 11 we can observe both retrievals with arrows pointing to~~

~~the identified plumesof each retrieval, which mainly are originated from venting shafts. There is a lower background noise and a lower number of retrieval artifacts when using Combo-MF. This helped to determine whether potential plumes that remained doubtful with~~ (green) retrievals. While the source in a is associated with a drainage station, in $b-d$ we observe emissions emanating from venting shafts. In addition, the masked clusters associated with the plumes, framed in red, are illustrated along with their surroundings. We can observe that the Combo-MF mask discards an important fraction of those clusters from the 2300-MF ~~were actually true plumes. As a result, while only 5 plumes were identified with~~ mask related to retrieval artifacts coming from surface structures such as roads or facilities. The clutter penalization from Combo-MF also reduces other pixel retrieved enhancements, resulting in a lower number of clusters related to background noise. However, clutter emergence does not always yields ΔXCH_4 values in SWIR-MF greater than those in 2300-MF and therefore they cannot be removed according to Eq. 9. Instead, these values are scaled, which contributes to the appeareance of undesired clusters. For instance, right below the plume in d, a small cluster that is not present in 2300-MF ~~, 15 plumes were detected with~~ appears in Combo-MF. In addition, the use of a more demanding target spectrum in Combo-MF can lead to the underestimation of weak plume pixels such as those from the plume tail. These pixels can be confused by background noise even after applying the scaling factor f. Therefore, plume clusters such as in c can present a more reduced shape than in 2300-MF. Altogether, we observe that there is a lower number of clusters around the plume when using Combo-MF, which facilitates plume detection.

4 Summary and conclusions

In this work, we propose a new matched filter-based ~~retrieval~~ procedure that attenuates or removes retrieval artifacts and also reduces the positive values of background noise, which leads to a greater capability for CH_4 emission detection. First, simulated CH_4 plumes have been implemented in different ~~data sets~~ PRISMA datasets and a visual comparison has been made. Second, we have done a quantification assessment ~~using different masking methods~~on the implemented synthetic plumes using masks derived from different retrievals. Third, the ~~disturbance~~ interference of H_2O and CO_2 in CH_4 retrievals has also been assessed by means of simulations ~~and analysis of real cases~~applied in PRISMA and EnMAP datasets. Finally, retrievals containing CH_4 ~~plumes~~ emissions from real AVIRIS-NG, ~~GF5-02 AHSI~~EnMAP, and PRISMA data ~~sets~~have been assessed in order to compare the proposed procedure to already existing procedures by means of an automatic detection algorithm and visual inspection.

~~Comparing Combo-MF to the common 2300-MF through simulated and not-simulated data sets from different missions, we find~~ Our analysis reveals that Combo-MF ~~reduces the positive background noise values and attenuates or even practically removes retrieval artifacts coming from topography or other structures, while keeping~~ effectively attenuates or practically removes an important fraction of retrieval artifacts, while maintaining plume ΔXCH_4 ~~levels from plumes. However, the interference of~~ values at levels comparable to those obtained with 2300-MF. In addition, plume masking resulting from Combo-MF is less affected by background noise for small flux rate values ($Q < 1000$ kg/h), which is translated in a lower sensitivity to clutter. Nevertheless, emissions over surface structures linked to artifacts can be considerably attenuated in the Combo-MF retrieval due to the penalization of the underlying surface, as seen in the Gazhipur landfill case. Moreover, local
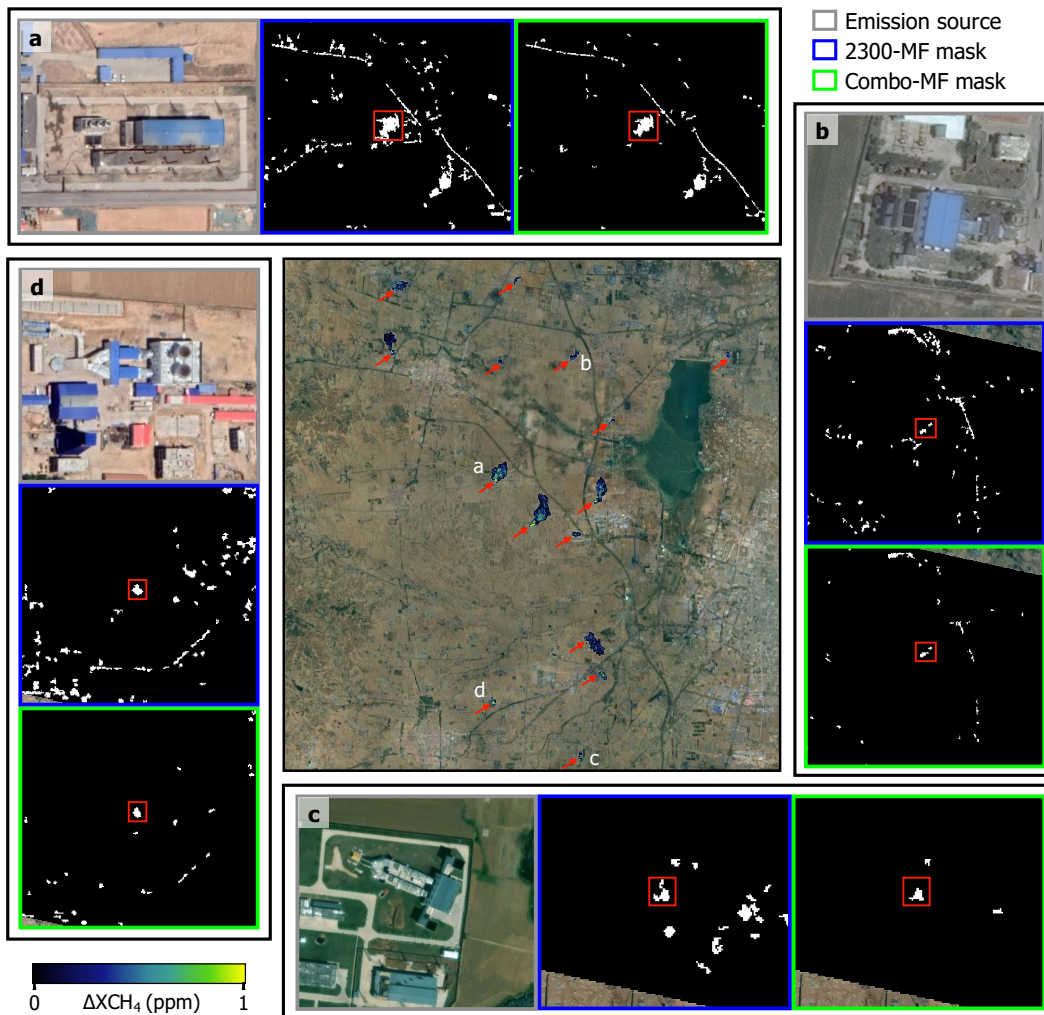
Figure 11. ~~True color image (left), 2300-MF retrieval (center), and Combo-MF retrieval~~ Plumes (~~right~~pointed out with red arrows) ~~from~~ detected using a PRISMA ~~data set~~ dataset from a coal mine site in Shanxi (China)~~showing~~, overlaid on a © Google Earth high-resolution image (central panel). At the ~~detected~~ edges, four blocks associated to plumes (~~marked with arrows~~labeled $a - d$) ~~with each procedure~~display a zoomed-in view of the emission source (gray) and of the output masks from the automatic detection algorithm. The masks shows the cluster related to the plume (framed in red) and their surroundings for the 2300-MF (blue) and Combo-MF (green) retrievals.

510 enhancements of H_2O or CO_2 ~~plumes~~ interfering with CH_4 emissions~~such as~~, as observed in inefficient flaring ~~can lead to an attenuation of~~ cases, can attenuate the plume enhancement in the ΔXCH_4 maps. ~~Regarding~~ On the other hand, atmospheric H_2O and CO_2 concentrations ~~, there is practically no disturbance in~~ have a negligible impact on the retrievals because of the ~~homogeneity~~ homogeneous distribution of these trace gases across the ~~scenes. We have also tested~~ retrieved area. We also

evaluated the performance of MAG1C ~~with~~ using the 1000-2500 nm spectral range~~and have found that there is a reduction~~, observing a reduction in the number of retrieval artifacts ~~in comparison~~ compared to the default 2122-2488 nm window. ~~MAG1C retrievals present a~~ Despite this reduced number and the lower background noise, ~~but also~~ it generates plumes with higher ~~score and~~ ΔXCH_4 values and still exhibits a greater number of ~~disturbing retrieval artifacts in comparison~~ artifacts compared to Combo-MF retrievals. Therefore, Combo-MF can be considered as an optimal trade-off between background noise ~~reduction~~ and retrieval artifact ~~attenuation, which leads to a better~~ reduction, which generally leads to an improved plume detection capability. This is illustrated by a comprehensive analysis in a PRISMA ~~data set from a coal mine site in China found 5 plumes using 2300-MF, but 15 when using Combo-MF. In addition, flux rate estimations from simulated plumes ranging from 200 to 5000 revealed that plume masking derived from Combo-MF could result in more accurate values than those derived from 2300-MF~~dataset, where the output masks from an automatic detection algorithm show an important reduction in the number of clusters not related to CH_4 emissions.

Data availability. Data will be made available on request.

Author contributions. **Javier Roger**: Conceptualization, Methodology, Formal analysis, Investigation, Writing – original draft, Writing – review & editing. **Luis Guanter**: Conceptualization, Resources, Writing – review & editing, Supervision. **Javier Gorroño**: Conceptualization, Methodology, Writing – review & editing. **Itziar Irakulis-Loitxate**: Formal Analysis, Resources, Writing – review & editing.

Competing interests. The authors declare that they have no conflict of interest.

Acknowledgements. The authors thank the Italian Space Agency, the DLR Space Agency, ~~the GaoFen team~~ and, JPL team for the PRISMA, EnMAP, ~~GaoFen-5, GaoFen-5-02,~~ and AVIRIS-NG data used in this work, respectively. We are grateful to Daniel J. Varon for the WRF-LES ~~modelled~~ modeled plumes used in this study. Authors Javier Roger, Javier Gorroño, and Luis Guanter received funding from ESA contract 4000134929.

References

Ayasse, A. K., Thorpe, A. K., Roberts, D. A., Funk, C. C., Dennison, P. E., Frankenberg, C., Steffke, A., and Aubrey, A. D.: Evaluating the effects of surface properties on methane retrievals using a synthetic airborne visible/infrared imaging spectrometer next generation (AVIRIS-NG) image, Remote Sensing of Environment, 215, 386 – 397, https://doi.org/https://doi.org/10.1016/j.rse.2018.06.018, 2018.

Ayasse, A. K., Thorpe, A. K., Cusworth, D. H., Kort, E. A., Negron, A. G., Heckler, J., Asner, G., and Duren, R. M.: Methane remote sensing and emission quantification of offshore shallow water oil and gas platforms in the Gulf of Mexico, Environmental Research Letters, 17, 084 039, https://doi.org/10.1088/1748-9326/ac8566, 2022.

Buchwitz, M., de Beek, R., Noël, S., Burrows, J. P., Bovensmann, H., Bremer, H., Bergamaschi, P., Körner, S., and Heimann, M.: Carbon monoxide, methane and carbon dioxide columns retrieved from SCIAMACHY by WFM-DOAS: year 2003 initial data set, Atmospheric Chemistry and Physics, 5, 3313–3329, , 2005.

C3S, C. D. S.: Carbon dioxide data from 2002 to present derived from satellite observations. Copernicus Climate Change Service (C3S) Climate Data Store (CDS), accessed: 31-05-2023), 10.24381/cds.f74805c87, 2018.

Cusworth, D., Thorpe, A., Miller, C., Ayasse, A., Jiorle, R., Duren, R., Nassar, R., Mastrogiacomo, J.-P., and Nelson, R.: Two years of satellite-based carbon dioxide emission quantification at the world's largest coal-fired power plants, EGUsphere, 2023, 1–35, https://doi.org/10.5194/egusphere-2023-1408, 2023.

Cusworth, D. H., Jacob, D. J., Varon, D. J., Chan Miller, C., Liu, X., Chance, K., Thorpe, A. K., Duren, R. M., Miller, C. E., Thompson, D. R., Frankenberg, C., Guanter, L., and Randles, C. A.: Potential of next-generation imaging spectrometers to detect and quantify methane point sources from space, Atmospheric Measurement Techniques, 12, 5655–5668, https://doi.org/10.5194/amt-12-5655-2019, 2019.

Dlugokencky, E.: https://gml.noaa.gov/ccgg/trends_ch4/, accessed: 2023-06-06, 2023.

Duren, R., Thorpe, A., Foster, K., Rafiq, T., Hopkins, F., Yadav, V., Bue, B., Thompson, D., Conley, S., Colombi, N., Frankenberg, C., McCubbin, I., Eastwood, M., Falk, M., Herner, J., Croes, B., Green, R., and Miller, C.: California's methane super-emitters, Nature, 575, 180–184, https://doi.org/10.1038/s41586-019-1720-3, 2019.

Eismann, M.: Hyperspectral Remote Sensing, vol. PM210 of *SPIE Press Monograph*, Society of Photo Optical, 2012.

Foote, M. D., Dennison, P. E., Thorpe, A. K., Thompson, D. R., Jongaramrungruang, S., Frankenberg, C., and Joshi, S. C.: Fast and Accurate Retrieval of Methane Concentration From Imaging Spectrometer Data Using Sparsity Prior, IEEE Transactions on Geoscience and Remote Sensing, 58, 6480–6492, 2020.

Foote, M. D., Dennison, P. E., Sullivan, P. R., O'Neill, K. B., Thorpe, A. K., Thompson, D. R., Cusworth, D. H., Duren, R., and Joshi, S. C.: Impact of scene-specific enhancement spectra on matched filter greenhouse gas retrievals from imaging spectroscopy, Remote Sensing of Environment, 264, 112 574, https://doi.org/https://doi.org/10.1016/j.rse.2021.112574, 2021.

Frankenberg, C., Platt, U., and Wagner, T.: Iterative maximum a posteriori (IMAP)-DOAS for retrieval of strongly absorbing trace gases: Model studies for CH_4 and CO_2 retrieval from near infrared spectra of SCIAMACHY onboard ENVISAT, Atmospheric Chemistry and Physics, 5, 9–22, https://doi.org/10.5194/acp-5-9-2005, 2005.

Frankenberg, C., Thorpe, A. K., Thompson, D. R., Hulley, G., Kort, E. A., Vance, N., Borchardt, J., Krings, T., Gerilowski, K., Sweeney, C., Conley, S., Bue, B. D., Aubrey, A. D., Hook, S., and Green, R. O.: Airborne methane remote measurements reveal heavy-tail flux distribution in Four Corners region, Proceedings of the National Academy of Sciences, 113, 9734–9739, https://doi.org/10.1073/pnas.1605617113, 2016.

570 Gordon, I., Rothman, L., Hill, C., Kochanov, R., Tan, Y., Bernath, P., Birk, M., Boudon, V., Campargue, A., Chance, K., Drouin, B., Flaud, J.-M., Gamache, R., Hodges, J., Jacquemart, D., Perevalov, V., Perrin, A., Shine, K., Smith, M.-A., Tennyson, J., Toon, G., Tran, H., Tyuterev, V., Barbe, A., Császár, A., Devi, V., Furtenbacher, T., Harrison, J., Hartmann, J.-M., Jolly, A., Johnson, T., Karman, T., Kleiner, I., Kyuberis, A., Loos, J., Lyulin, O., Massie, S., Mikhailenko, S., Moazzen-Ahmadi, N., Müller, H., Naumenko, O., Nikitin, A., Polyansky, O., Rey, M., Rotger, M., Sharpe, S., Sung, K., Starikova, E., Tashkun, S., Auwera, J. V., Wagner, G., Wilzewski, J., Wcisło, P.,
575 Yu, S., and Zak, E.: The HITRAN2016 molecular spectroscopic database, Journal of Quantitative Spectroscopy and Radiative Transfer, 203, 3–69, , hITRAN2016 Special Issue, 2017.

Guanter, L., Segl, K., Sang, B., Alonso, L., Kaufmann, H., and Moreno, J.: Scene-based spectral calibration assessment of high spectral resolution imaging spectrometers, Opt. Express, 17, 11 594–11 606, https://doi.org/10.1364/OE.17.011594, 2009.

Guanter, L., Kaufmann, H., Segl, K., Foerster, S., Rogass, C., Chabrillat, S., Kuester, T., Hollstein, A., Rossner, G., Chlebek,
580 C., and et al.: The EnMAP Spaceborne Imaging Spectroscopy Mission for Earth Observation, Remote Sensing, 7, 8830–8857, https://doi.org/10.3390/rs70708830, 2015.

Guanter, L., Irakulis-Loitxate, I., Gorroño, J., Sánchez-García, E., Cusworth, D. H., Varon, D. J., Cogliati, S., and Colombo, R.: Mapping methane point emissions with the PRISMA spaceborne imaging spectrometer, Remote Sensing of Environment, 265, 112 671, https://doi.org/https://doi.org/10.1016/j.rse.2021.112671, 2021.

585 Irakulis-Loitxate, I., Guanter, L., Liu, Y.-N., Varon, D. J., Maasakkers, J. D., Zhang, Y., Chulakadabba, A., Wofsy, S. C., Thorpe, A. K., Duren, R. M., Frankenberg, C., Lyon, D. R., Hmiel, B., Cusworth, D. H., Zhang, Y., Segl, K., Gorroño, J., Sánchez-García, E., Sulprizio, M. P., Cao, K., Zhu, H., Liang, J., Li, X., Aben, I., and Jacob, D. J.: Satellite-based survey of extreme methane emissions in the Permian basin, Science Advances, 7, https://doi.org/10.1126/sciadv.abf4507, 2021.

Jervis, D., McKeever, J., Durak, B. O. A., Sloan, J. J., Gains, D., Varon, D. J., Ramier, A., Strupler, M., and Tarrant, E.: The GHGSat-D
590 imaging spectrometer, Atmospheric Measurement Techniques, 14, 2127–2140, https://doi.org/10.5194/amt-14-2127-2021, 2021.

Knapp, M., Scheidweiler, L., Külheim, F., Kleinschek, R., Necki, J., Jagoda, P., and Butz, A.: Spectrometric imaging of sub-hourly methane emission dynamics from coal mine ventilation, Environmental Research Letters, 18, https://doi.org/10.1088/1748-9326/acc346, 2023.

Liu, Y., Sun, D., Hu, X., Ye, X., Li, Y., Liu, S., Cao, K., Chai, M., Zhou, W., Zhang, J., Zhang, Y., Sun, W., and Jiao, L.: The Advanced Hyperspectral Imager: Aboard China's GaoFen-5 Satellite, IEEE Geoscience and Remote Sensing Magazine, 7, 23–32, 2019.

595 Loizzo, R., Guarini, R., Longo, F., Scopa, T., Formaro, R., Facchinetti, C., and Varacalli, G.: Prisma: The Italian Hyperspectral Mission, pp. 175–178, https://doi.org/10.1109/IGARSS.2018.8518512, 2018.

Lou, H., Zhang, J., Yang, S., Cai, M., Ren, X., Luo, Y., and Li, C.: Exploring the Relationships of Atmospheric Water Vapor Contents and Different Land Surfaces in a Complex Terrain Area by Using Doppler Radar, Atmosphere, 12, https://doi.org/10.3390/atmos12050528, 2021.

600 Manolakis, D., Lockwood, R., Cooley, T., and Jacobson, J.: Robust Matched Filters for Target Detection in Hyperspectral Imaging Data, in: 2007 IEEE International Conference on Acoustics, Speech and Signal Processing - ICASSP '07, vol. 1, pp. I–529–I–532, https://doi.org/10.1109/ICASSP.2007.366733, 2007.

Masood, F., Ahmad, S., and Malik, A.: Role of Methanotrophs in Mitigating Global Warming, pp. 43–60, Springer Singapore, Singapore, https://doi.org/10.1007/978-981-33-4508-9_4, 2021.

605 Mayfield, E. N., Robinson, A. L., and Cohon, J. L.: System-wide and Superemitter Policy Options for the Abatement of Methane Emissions from the U.S. Natural Gas System, Environmental Science & Technology, 51, 4772–4780, https://doi.org/10.1021/acs.est.6b05052, pMID: 28195720, 2017.

Mieruch, S., Schröder, M., Noël, S., and Schulz, J.: Comparison of decadal global water vapor changes derived from independent satellite time series, Journal of Geophysical Research: Atmospheres, 119, 12,489–12,499, https://doi.org/https://doi.org/10.1002/2014JD021588, 2014.

Ming, T., Li, W., Yuan, Q., Davies, P., de Richter, R., Peng, C., Deng, Q., Yuan, Y., Caillol, S., and Zhou, N.: Perspectives on removal of atmospheric methane, Advances in Applied Energy, 5, 100 085, https://doi.org/https://doi.org/10.1016/j.adapen.2022.100085, 2022.

Molod, A., Takacs, L., Suarez, M., Bacmeister, J., Song, I.-S., and Eichmann, A.: The GEOS-5 Atmospheric General Circulation Model: Mean Climate and Development from MERRA to Fortuna, https://portal.nccs.nasa.gov/datashare/gmao/geos-fp/das/, nASA TM-2012-104606, 2012, 2012.

Ocko, I. B., Sun, T., Shindell, D., Oppenheimer, M., Hristov, A. N., Pacala, S. W., Mauzerall, D. L., Xu, Y., and Hamburg, S. P.: Acting rapidly to deploy readily available methane mitigation measures by sector can immediately slow global warming, Environmental Research Letters, 16, 054 042, https://doi.org/10.1088/1748-9326/abf9c8, 2021.

Roger, J., Irakulis-Loitxate, I. Valverde, A., Gorroño, J., Chabrillat, S., Brell, M., and Guanter, L.: High-resolution methane mapping with the EnMAP satellite imaging spectroscopy mission [Preprint], https://doi.org/https://doi.org/10.31223/X5M65Z, 2023.

Spectral Sciences, Inc.: http://modtran.spectral.com/, 2016.

Thompson, D. R., Leifer, I., Bovensmann, H., Eastwood, M., Fladeland, M., Frankenberg, C., Gerilowski, K., Green, R. O., Kratwurst, S., Krings, T., Luna, B., and Thorpe, A. K.: Real-time remote detection and measurement for airborne imaging spectroscopy: a case study with methane, Atmospheric Measurement Techniques, 8, 4383–4397, https://doi.org/10.5194/amt-8-4383-2015, 2015.

Thompson, D. R., Thorpe, A. K., Frankenberg, C., Green, R. O., Duren, R., Guanter, L., Hollstein, A., Middleton, E., Ong, L., and Ungar, S.: Space-based remote imaging spectroscopy of the Aliso Canyon CH4 superemitter, Geophysical Research Letters, 43, 6571–6578, https://doi.org/10.1002/2016GL069079, 2016.

Thorpe, A. K., Roberts, D. A., Bradley, E. S., Funk, C. C., Dennison, P. E., and Leifer, I.: High resolution mapping of methane emissions from marine and terrestrial sources using a Cluster-Tuned Matched Filter technique and imaging spectrometry, Remote Sensing of Environment, 134, 305–318, https://doi.org/https://doi.org/10.1016/j.rse.2013.03.018, 2013.

Thorpe, A. K., Frankenberg, C., and Roberts, D. A.: Retrieval techniques for airborne imaging of methane concentrations using high spatial and moderate spectral resolution: application to AVIRIS, Atmospheric Measurement Techniques, 7, 491–506, https://doi.org/10.5194/amt-7-491-2014, 2014.

Thorpe, A. K., Frankenberg, C., Thompson, D. R., Duren, R. M., Aubrey, A. D., Bue, B. D., Green, R. O., Gerilowski, K., Krings, T., Borchardt, J., Kort, E. A., Sweeney, C., Conley, S., Roberts, D. A., and Dennison, P. E.: Airborne DOAS retrievals of methane, carbon dioxide, and water vapor concentrations at high spatial resolution: application to AVIRIS-NG, Atmospheric Measurement Techniques, 10, 3833–3850, https://doi.org/10.5194/amt-10-3833-2017, 2017.

UNEP: Global Methane Assessment: Benefits and Costs of Mitigating Methane Emissions, https://www.unep.org/resources/report/global-methane-assessment-benefits-and-costs-mitigating-methane-emissions, 2021.

Varon, D. J., Jacob, D. J., McKeever, J., Jervis, D., Durak, B. O. A., Xia, Y., and Huang, Y.: Quantifying methane point sources from fine-scale satellite observations of atmospheric methane plumes, Atmospheric Measurement Techniques, 11, 5673–5686, https://doi.org/10.5194/amt-11-5673-2018, 2018.